Protein cofactors and substrate influence Mg²⁺-dependent structural changes in the catalytic RNA of archaeal RNase P

Ila A. Marathe [ID][1,2,3], **Stella M. Lai** [ID][2,3,4,†], **Walter J. Zahurancik** [ID][2,3,†], **Michael G. Poirier** [ID][2,3,5], **Vicki H. Wysocki** [ID][2,3,4] and **Venkat Gopalan** [ID][1,2,3,*]

[1]Department of Microbiology, The Ohio State University, Columbus, OH 43210, USA, [2]Department of Chemistry and Biochemistry, The Ohio State University, Columbus, OH 43210, USA, [3]Center for RNA Biology, The Ohio State University, Columbus, OH 43210, USA, [4]Resource for Native Mass Spectrometry-Guided Structural Biology, The Ohio State University, Columbus, OH 43210, USA and [5]Department of Physics, The Ohio State University, Columbus, OH 43210, USA

ABSTRACT

The ribonucleoprotein (RNP) form of archaeal RNase P comprises one catalytic RNA and five protein cofactors. To catalyze Mg²⁺-dependent cleavage of the 5′ leader from pre-tRNAs, the catalytic (C) and specificity (S) domains of the RNase P RNA (RPR) cooperate to recognize different parts of the pre-tRNA. While ∼250–500 mM Mg²⁺ renders the archaeal RPR active without RNase P proteins (RPPs), addition of all RPPs lowers the Mg²⁺ requirement to ∼10–20 mM and improves the rate and fidelity of cleavage. To understand the Mg²⁺- and RPP-dependent structural changes that increase activity, we used pre-tRNA cleavage and ensemble FRET assays to characterize inter-domain interactions in *Pyrococcus furiosus* (*Pfu*) RPR, either alone or with RPPs ± pre-tRNA. Following splint ligation to doubly label the RPR (Cy3-RPR_C domain and Cy5-RPR_S domain), we used native mass spectrometry to verify the final product. We found that FRET correlates closely with activity, the *Pfu* RPR and RNase P holoenzyme (RPR + 5 RPPs) traverse different Mg²⁺-dependent paths to converge on similar functional states, and binding of the pre-tRNA by the holoenzyme influences Mg²⁺ cooperativity. Our findings highlight how Mg²⁺ and proteins in multi-subunit RNPs together favor RNA conformations in a dynamic ensemble for functional gains.

INTRODUCTION

Ribonucleoproteins (RNPs) are essential for fundamental cellular processes (e.g., mRNA splicing, RNA process-

ing, translation). However, our understanding of how RNA structural changes induced by protein binding control the functional repertoire of complex RNPs is limited but growing. In some RNPs, this cooperation is required because proteins help RNAs overcome their weak affinity for sparse intracellular Mg²⁺, while in others proteins may either stabilize or nudge the RNA towards the native fold necessary for function ([1–18]). These advances, especially in the context of small RNPs, together with our increasing knowledge of RNA-protein interaction principles ([19]), provide a foundation to investigate the functional coupling between multiple components in larger RNPs. Nevertheless, because function often requires assembly of the entire RNP ([20,21]), establishing structure-function relationships for intermediate sub-complexes can be difficult even when detailed maps of the assembly pathway are available. In this regard, because archaeal and eukaryotic RNase P sub-assemblies have fractional activity ([22–30]), they are good models for studying large, multi-subunit RNPs as functional payoffs from RNA-protein cooperation can be dissected in a stepwise fashion.

The 5′-processing of precursor tRNAs (pre-tRNAs) mediated by the RNP form of RNase P is due to a single catalytic RNase P RNA (RPR) subunit that associates with a variable number of RNase P protein (RPP) subunits: one in Bacteria, up to five in Archaea, and up to 10 in Eukarya (nucleus) ([31–36]). This diversity in the overall makeup of the different RNase P RNP variants masks the striking conservation of the RPR's active site, which remains constant even in the context of different auxiliary structural elements ([32–35]). In the absence of RPPs, many RPRs show weak activity in the presence of elevated concentrations of Mg²⁺, an essential cofactor ([24,25,29,30,37]). The crystal structure of bacterial RNase P ([38]) and the cryo-EM structures of archaeal and eukaryotic RNase P ([39–41]) provide high-resolution details about the arrangement

*To whom correspondence should be addressed. Fax: +1 614 292 6773; Email: gopalan.5@osu.edu
†The authors wish it to be known that, in their opinion, these two authors should be regarded as joint Second Authors.

of individual subunits and, importantly, highlight the uniformity amidst their diversity. They confirm findings from biochemical studies that all RPRs are modular in having a catalytic (C) domain that cleaves the 5′ leader of pre-tRNAs and a specificity (S) domain that binds the 'elbow' structure of the L-shaped tRNA (24,25,42,43). Conserved inter-domain interactions act as braces to forge RPR structures that can simultaneously recognize different parts of the pre-tRNA substrate (Supplementary Figure S1). For example, the long-range interaction between a GNRA tetraloop in the S domain and its dock site on the P1 (paired region 1) helix in the C domain is present in all RPRs (40,41,44,45).

The five archaeal RPPs (RPP21, RPP29, POP5, RPP30 and L7Ae; see (46) for an exception) are homologous to eukaryotic RPPs (47), allowing archaeal RNase P to serve as a surrogate for its more intractable eukaryotic cousin (25,48,49). Our *in vitro* reconstitutions of RNase P from different archaea (22,24–26) showed that RPP21•RPP29 and POP5•RPP30 work in pairs with the RPR to yield partial RNPs that are catalytically intermediate between the RPR alone and holoenzymes containing all RPPs (22,24,25). These binary complexes distinctly enhance the RPR's apparent substrate affinity and rate of cleavage (22) while also synergistically rescuing mis-cleavage of non-canonical pre-tRNAs (23). Together, these four RPPs enable uniform cleavage of substrates that are otherwise processed at vastly different rates by the RPR alone. L7Ae, the fifth RPP, binds kink-turns in the RPR and potentiates archaeal RNase P function (7,26,27,50). To understand how the binding of different RPPs to specific regions of the RPR independently and collectively mediate structural changes that are essential for assembly and cleavage of diverse substrates, we focus on the interplay between Mg^{2+} and induced fit in *Pyrococcus furiosus* (*Pfu*) RNase P, an archaeal variant that we have previously characterized using biochemical, footprinting, and native mass spectrometry experiments (7,25,50,51).

Mg^{2+} plays two different roles in RNA function. First, diffuse, outer-sphere interactions as well as specific, inner-sphere interactions with Mg^{2+} help shape the tertiary structure of RNAs (52,53). Second, Mg^{2+} is essential for the activity of ribozymes including RNase P due to its involvement in a two metal-ion mechanism for phosphoryl transfer (37,54–56). While *Pfu* RPR alone in 500 mM Mg^{2+} and at 55°C is weakly active (25), addition of RPPs significantly decreases the Mg^{2+} requirement and enhances catalytic efficiency. POP5•RPP30 and RPP21•RPP29 independently decrease the Mg^{2+} requirement from 500 mM to 120 mM, and further decrease the requirement to 30 mM when working together (25). Additionally, inclusion of L7Ae decreases this amount to ~10 mM for the 5-RPP combination (7). In most ribozymes, the roles of Mg^{2+} in structure and function are likely coupled.

Results from multiple kinetic studies point to a conformational change from the enzyme-substrate (ES) ground state to an activated ES* state before pre-tRNA cleavage. First, readout of the invariant tRNA 'elbow' by the S domain in bacterial and archaeal RPRs somehow rearranges the active site in the C domain. This inter-domain signaling, which modulates the location and affinity for catalytically relevant Mg^{2+}, appears to be mediated by the substrate and

constitutes an important determinant for rate and cleavage-site selection (24,57–60). Second, time-course analyses of the binding of a fluor-labeled pre-tRNA to *Bacillus subtilis* RNase P displayed biphasic kinetics, with an initial diffusion-limited encounter followed by a conformational change prior to cleavage (61). Third, kinetic studies with bacterial and archaeal RNase P suggest that the RPP(s) engender similar cleavage rates for different pre-tRNAs by shifting the equilibrium of the pre-cleavage isomerization from ES to ES* (22,24,62,63).

Despite the above findings, which suggest an induced-fit mechanism for RNase P, structural studies thus far indicate that the enzyme is largely pre-organized for catalysis. Superposition of the structures of *Methanocaldococcus jannaschii* (*Mja*) RNase P obtained in the absence or presence of tRNA^{Tyr} did not show any substantive differences in the conformation of the RPR or RPPs (40); the same scenario was observed with bacterial RNase P (38), although subsequent SAXS studies of three phylogenetically distinct bacterial RPRs (64) suggested that conformational properties in solution may have been masked in the crystal due to specific inter-/intra-molecular interactions. Interestingly, cryo-EM structures of *Saccharomyces cerevisiae* RNase P in the absence or presence of pre-tRNA^{Phe} revealed that a universally conserved uridine (U93) rotates drastically and points into the active site to coordinate and position a Mg^{2+} ion for pre-tRNA cleavage. Molecular dynamics (MD) simulations also showed that U93 has a dynamic conformation in the holoenzyme (RPR + 5 RPPs) but is constrained upon binding to the pre-tRNA (39).

Since Förster resonance energy transfer (FRET) measurements in solution have been employed to obtain dynamic information about RNA folding and RNP assembly (4,6,10,11,13,15,18,65), we sought to use FRET for identifying conformational changes during RNase P catalysis that may be inaccessible to cryo-EM- and X-ray crystallography-based snapshots. Specifically, our goal was to monitor Mg^{2+}-induced, large-scale conformational changes in the *Pfu* RPR (± RPPs) and to investigate how these structural alterations correlate with the pre-tRNA cleavage activity of *Pfu* RNase P. Although our ensemble studies cannot shed light on either fast or slow movement(s) of specific residues/domains, we expected to gain insights into RPR conformational ensembles under equilibrium conditions. Indeed, our results highlight how Mg^{2+} promotes tertiary interactions between the *Pfu* RPR's C and S domains that are important for dual anchoring of the pre-tRNA substrate and remodels the *Pfu* RNase P holoenzyme. Our findings have implications for understanding the assembly of multi-subunit, cellular RNPs.

MATERIALS AND METHODS

Cloning of *Pfu* RPR 5′3′ext, *Pfu* RPR ext mP1 and *Thermus thermophilus* (*Tth*) pre-tRNA^{Gly}

The protocols for cloning the *Pfu* RPR derivatives and pre-tRNA used in the studies reported here are described in the *Supplementary Information* (see Supplementary Table S1 for information on oligonucleotides used for cloning). All RNAs were generated by T7 RNA polymerase (T7 RNAP)-mediated run-off *in vitro* transcription (IVT) using as tem-

plates either linearized plasmid DNA or a PCR amplicon that included the T7 RNAP promoter (see *Supplementary Information*). As to nomenclature: *Pfu* RPR 5′3′ext refers to a *Pfu* RPR variant containing 23-nt extensions at both termini; *Pfu* RPR ext mP1 contains the extensions in *Pfu* RPR 5′3′ext and in addition lacks the two native terminal bp in P1.

Native MS analysis

All native MS experiments were conducted using a Q Exactive™ Ultra-High Mass Range (UHMR) Hybrid Quadrupole-Orbitrap™ mass spectrometer (Thermo Scientific) that was modified with a customized device for performing surface-induced dissociation (66,67). Samples were diluted to 1 μM in 800 mM NH₄OAc and transferred to filament-containing borosilicate glass capillary tips (Sutter Instrument, Novato, CA) that were individually pulled in-house using a P-97 micropipette puller (Sutter Instrument). A platinum wire was then inserted into the sample solution, and a voltage of 0.7–1.5 kV was applied to directly infuse the sample into the UHMR mass spectrometer by nano-electrospray ionization. An in-source trapping voltage of -100 to -200 V and capillary temperature of 250°C were also applied to aid desolvation. Other instrument tune settings were as follows: scan range, 350–10,000 m/z; resolution (at 400 m/z), 3,125; microscans, 5; maximum injection time, 200 ms; S-lens radio frequency (RF) level, 200 V; source direct current (DC) offset, 21 V; injection flatapole DC, 9 V; inter flatapole DC, 8 V; bent flatapole DC, 6 V; transfer multipole DC, 0 V; C-trap entrance lens offset, 1.8 V; trapping gas pressure setting, 4. For all RNAs, except the synthetic internal fragment oligonucleotide, the mass spectrometer was set to high m/z ion transfer mode, with RF amplitudes of 700, 940 and 900 V applied to the injection flatapole, bent flatapole, and transfer multipole/higher-energy collisional dissociation cell, respectively; RF amplitudes of 150, 300 and 250 V, respectively, were used for the I-F oligonucleotide samples, which were analyzed in low m/z ion transfer mode.

Microscale thermophoresis (MST)

Equilibrium dissociation constants (K_D) for binding of 5′-ext-Cy5–oligo (referred hereafter as Cy5–oligo; Supplementary Table S2, Millipore Sigma) to the 5′ extension of unlabeled *Pfu* RPR ext mP1 in the absence or presence of *Pfu* RPPs were determined using MST. All MST measurements were collected using a Monolith Pico instrument (NanoTemper Technologies, San Francisco, CA) and standard NanoTemper glass capillaries (MO-K022). Final 20-μl binding reactions containing 0.75 nM Cy5–oligo were incubated for 10 min at 37°C before initiating MST measurements.

Pfu RPR ext mP1 alone. *Pfu* RPR ext mP1 was folded in the presence of 10 mM MgCl₂, serially diluted 1:1 in the appropriate 1× folding buffer (see below) and mixed with Cy5–oligo for a final Mg²⁺ concentration of either 10 or 500 mM.

Pfu RPR ext mP1 + 5 RPPs. *Pfu* RPR ext mP1 was folded in the presence of 2.5 mM MgCl₂ and sequentially incubated for 5 min at 37°C with a 10-fold molar excess each of RPP21•RPP29, then L7Ae, and finally POP5•RPP30. Upon assembly of the holoenzyme, it was serially diluted 1:1 in Mg²⁺-free buffer and mixed with Cy5–oligo for a final Mg²⁺ concentration of either 0.033 or 30 mM.

During MST measurements, excitation power was set to 15% while MST power was set to medium. Initial fluorescence was measured for 5 s before the infrared laser was turned on for 30 s. Fluorescence was then monitored for an additional 5 s after the infrared laser was turned off. Data from MST measurements were plotted using Kaleidagraph (Synergy Software). K_D values were calculated by plotting ΔF_{Norm} versus the concentration of either *Pfu* RPR ext mP1 or *Pfu* RPR ext mP1 + 5 RPPs and by fitting the data to hyperbolic binding isotherms. Mean and standard deviation values for each condition were calculated from three technical replicates. Curve-fit errors did not exceed 25% in any trial.

RNase P activity assays

All activity assays and RNA folding were carried out in a thermal cycler (Bio-Rad, Formerly MJ Research Inc., Hercules, CA) and buffers sterilized using 0.22-μm syringe filters (VWR international, Radnor, PA). Separate assay buffers were prepared and pH-adjusted for each [Mg²⁺] tested. Prior to initiating cleavage assays, the RPR was incubated in ddH₂O for 50 min at 50°C and 10 min at 37°C before an equal volume of appropriate 2X folding buffer was added. The RNA sample was then incubated for an additional 30 min at 37°C. Composition of the 2X folding buffer varied depending on whether RPR alone or RPR + 5 RPP complex was used. Refolded RPR was added to buffer containing appropriate [Mg²⁺] and, where appropriate, reconstituted with the RPPs. Cleavage was initiated by adding the appropriate substrate.

Pfu RPR ext mP1 alone. Activity of the RPR alone was tested at 50-mM intervals from 100 to 500 mM Mg²⁺. Prior to cleavage assays, RPR was refolded in a 0.5-ml PCR tube (Thermo Fisher or Axygen) by first incubating in ddH₂O for 50 min at 50°C and for 10 min 37°C. Subsequently, the RPR was supplemented with an equal volume of 2X refolding buffer (100 mM HEPES–KOH [pH 8.4 at 25°C], 1.6 M NH₄OAc, 20 mM MgCl₂) and incubated for 30 min at 37°C. The final RPR concentration after refolding was 6 μM. First, 4.2 μl of 6 μM (for assays in 100–200 mM Mg²⁺) or 1.5 μM (for assays in 250–500 mM Mg²⁺) folded RPR were added to 6.3 μl 2× assay buffer and incubated for 2 min at 37°C. Each 2× buffer contained 50 mM HEPES–KOH (pH 8.4 at 25°C), 3.2 M NH₄OAc, 5% (w/v) PEG 8000 and varying concentrations of MgCl₂ (ranging from 190 to 990 mM). *Tth* pre-tRNA^{Gly}, a trace amount of which was labeled using 5′-γ-[³²P]-ATP (PerkinElmer, Shelton, CT) and T4 PNK (NEB), was diluted in 1X refolding buffer to a final concentration of 720 μM. Substrate cleavage was initiated by addition of 2.1 μl of 720 μM *Tth* pre-tRNA^{Gly}, which had been pre-incubated for 2 min at 37°C. The final assay volume of 12.6 μl contained 2 μM (for assays in 100–200

mM Mg^{2+}) or 0.5 µM (for assays in 250–500 mM Mg^{2+}) RPR and 120 µM *Tth* pre-tRNA^{Gly} in 1X buffers (50 mM HEPES [pH 8.4 at 25°C], 2 M NH$_4$OAc, 2.5% (w/v) PEG 8000 and 100–500 mM MgCl$_2$). After addition of substrate, the reaction mixture was briefly vortexed and centrifuged for a few seconds before returning to the thermal cycler. After defined time intervals dictated by [Mg^{2+}], 3-µl aliquots were removed from the reaction master mix and quenched with 17 µl loading dye. Cleavage products were separated using 10% (w/v) polyacrylamide/7 M urea gels. *Tth* pre-tRNA^{Gly} cleaved with *Escherichia coli* (*Eco*) RNase P was used as a positive control for RNase P cleavage.

During the first trial for each [Mg^{2+}] tested, a sample containing only the substrate in assay buffer was also incubated for the entire duration of the time course to determine the extent of uncatalyzed breakdown. In the majority of cases, the extent of uncatalyzed breakdown was found to be negligible (<4%). For subsequent trials, one sample containing the substrate alone was incubated for only the longest time period in the time-course assay. These samples were used as negative controls. Initial velocities did not change whether or not the nominal uncatalyzed background cleavage was subtracted.

Pfu RPR ext mP1 + 5 RPPs. Activity assays using *Pfu* RPR ext mP1 + 5 RPPs were performed in a manner similar to the RPR alone assays, albeit with some differences. A 2X refolding buffer containing only 5 mM MgCl$_2$ was used to accommodate the lower [Mg^{2+}] tested in the assays with RPR + 5 RPPs. RPPs were purified as described elsewhere (25,50). First, 1.64 µl of 500 nM RPR was added to 8.2 µl assay buffer containing varying [Mg^{2+}] and incubated for 5 min at 37°C. To reconstitute the RNP, RPR was mixed with 1.64 µl of 5 µM RPPs (in a specific order) and incubated for 5 min at 37°C following each addition. The order of addition was RPP21•RPP29, followed by L7Ae (C71V variant (50)), and finally POP5•RPP30. Due to the weak activity of the RPR + 5 RPPs with *Tth* pre-tRNA^{Gly} at 37°C, *Eco* pre-tRNA^{Tyr} (68) was used as the substrate for assays using RPR + 5 RPPs. Unlabeled *Eco* pre-tRNA^{Tyr} was mixed with a trace amount of 5′-[^{32}P]-pre-tRNA^{Tyr} and diluted to the desired final concentration in 100 mM HEPES–KOH (pH 8.4 at 25°C), 1.6 M NH$_4$OAc. To initiate pre-tRNA cleavage, 1.64 µl of 10 µM *Eco* pre-tRNA^{Tyr}, which had been pre-incubated at 37°C for 2 min, was added before the reaction was mixed by pipetting, briefly centrifuged, and returned to the thermal cycler. Each 16.4-µl assay contained 50 nM RPR, 500 nM RPPs and 1 µM *Eco* pre-tRNA^{Tyr}, in 1X assay buffer [50 mM HEPES (pH 8.4 at 25°C), 800 M NH$_4$OAc, 0.5–30 mM MgCl$_2$, and 2.5% (v/v) PEG 8000]. After defined time intervals dictated by [Mg^{2+}] used in each assay, 4-µl aliquots were withdrawn from the reaction master mix and quenched with 16 µl loading dye. Samples were analyzed by electrophoresis on 8% (w/v) polyacrylamide/7 M urea gels. *Eco* pre-tRNA^{Tyr} cleaved by *Eco* RNase P was used as positive control for RNase P cleavage. Negative controls were prepared as described above for the RPR-alone reactions.

Data analysis. Polyacrylamide gels were scanned using a Typhoon RGB imager (Cytiva) and were quantitated using ImageQuant (Cytiva). Percent cleavage values were plotted against the time of incubation to obtain the slope (initial velocity), which in turn was used for subsequent turnover number calculations. Time courses were designed to ensure 30–40% cleavage and maintain linearity in product formation. While there were a few reactions that exceeded this threshold marginally, all curve fits yielded correlation coefficients (R^2) > 0.96.

Ensemble FRET experiments

Buffers used for FRET experiments were identical to those used for activity assays. Cy5–*Pfu* RPR ext mP1 was mixed with a Cy3–labeled oligonucleotide (5′-ext-Cy3–oligo, referred hereafter as Cy3–oligo; Supplementary Table S2) complementary to the RPR's 5′ extension, and folding was performed as described above. Folded RPR + Cy3–oligo samples were added to the appropriate buffers (± RPPs) and pre-incubated at 37°C prior to FRET measurements. RPR, RPP, and substrate concentrations were identical to those used in activity assays unless otherwise stated, and each FRET sample had a final volume of 55 µl.

Pfu RPR ext mP1 alone. Folded RPR + Cy3–oligo samples were diluted to a final concentration of 100 nM Cy5–RPR ext mP1 + 77 nM Cy3–oligo prior to preincubation at 37°C. Samples were pre-incubated for 10 min at 37°C prior to FRET measurements. Although we had intended to use 100 nM of Cy3–oligo, we discovered that the concentration used was sub-stochiometric (77 nM) due to an error in the stock concentration. Fortuitously, the lower concentration of Cy3–oligo, which we continued to use, minimized leakage of donor into acceptor channels.

Pfu RPR ext mP1 + 5 RPPs. Enzyme reconstitution conditions, including order of RPP addition and incubation time, were identical to those used for activity assays. Samples contained 50 nM Cy5–RPR ext mP1, 500 nM RPPs, and 100 nM Cy3–oligo. In addition to the Mg^{2+} concentrations tested in activity assays, FRET measurements were also collected at 0.033, 0.1 and 0.25 mM Mg^{2+}. Samples were pre-incubated for 5 min at 37°C prior to FRET measurements.

Pfu RPR ext mP1 + 5 RPPs + pre-tRNA^{Tyr}. For measurements conducted in the presence of *Eco* pre-tRNA^{Tyr}, each sample contained 50 nM Cy5-RPR, 500 nM RPPs and 38.5 nM Cy3-oligo. We decreased the Cy3-oligo concentration to minimize potential non-specific binding of the Cy3–oligo to the excess pre-tRNA. However, two control experiments in which the Cy3–oligo concentration was varied revealed that Mg^{2+} dependent changes in E$_{FRET}$ were nearly identical when we added either 38.5 or 100 nM Cy3–oligo to *Pfu* RNase P in the absence or presence of substrate. Given the high affinity of the Cy3–oligo for the RPR (see below), we expect only a modest change in the concentration of bound species whether 38.5 or 100 nM Cy3–oligo was used. Following reconstitution, pre-incubated *Eco* pre-tRNA^{Tyr} was added to a final concentration of 1 µM and FRET was measured immediately to minimize substrate turnover.

Fluorescence and FRET measurements. Pre-incubated samples were transferred to a 45-µl Starna Cells cuvette (16.45F-Q3/Z8.5), and fluorescence was measured at 37°C using a Horiba PTI Quantamaster fluorometer. Excitation and emission slits were set to 5 nm each, and a lamp intensity correction was applied as per the manufacturer's instructions. The excitation wavelength was first set to 510 nm (for Cy3) and emission was measured from 530 to 750 nm. Next, the excitation wavelength was set to 610 nm (for Cy5) and emission was measured from 630 to 750 nm. For each sample, a blank measurement of buffer alone was also taken. The Ratio A method (69) was used to calculate FRET efficiencies using an automated MATLAB script (70).

RESULTS

Site-specific fluor labeling of *Pfu* RPR ext mP1

To conduct FRET measurements on the *Pfu* RPR, we sought to introduce the donor (Cy3) and the acceptor (Cy5) fluors in its C and S domains, respectively (Figure 1). While Cy3 was positioned on the C domain by virtue of a modified oligonucleotide that is complementary to an engineered extension, Cy5 was introduced in the S domain using a splint-ligation approach (Figures 1 and 2). For the latter, we synthesized three fragments of the *Pfu* RPR ext mP1: 5′-fragment (5-F, 1–183); internal fragment (I-F, 184–203); and 3′-fragment (3-F, 204–379) (Figure 2A). While 5-F and 3-F were made by IVT, I-F was chemically synthesized and obtained commercially. These three RNAs were then ligated using a DNA splint and T4 RNA ligase 2. Each fragment was processed individually and native MS was used to verify the mass of all components of the ligation reaction (Figure 2B–D; Supplementary Figure S2A-F; Supplementary Table S3; see *Supplementary Information* for additional experimental details).

Establishing the utility of doubly fluor-labeled *Pfu* RPR ext mP1 for FRET

To prepare the RPR for ensemble FRET experiments, the RNA was refolded in the presence of the Cy3–oligo that is complementary to the 5′-extension of the RPR. To ensure that the observed FRET changes are due to structural reorganization caused by Mg^{2+} or RPP binding and are not from potentially altered binding of the Cy3–oligo to the 5′-extension, we performed microscale thermophoresis (MST) experiments to measure the binding affinity of Cy3–oligo to *Pfu* RPR at low and high Mg^{2+} concentrations and either in the absence or presence of RPPs. Due to MST instrument specifications, we used an oligonucleotide identical in sequence to that used in our FRET studies but labeled with Cy5 instead of Cy3 (Supplementary Table S2). In the absence of RPPs, we determined K_D values of 4.3 ± 1.0 and 6.3 ± 0.6 nM at 10 mM and 500 mM Mg^{2+}, respectively (Figure 3A). In the presence of RPPs, the K_D value decreased modestly from 2.9 ± 0.4 nM at 0.033 mM Mg^{2+} to 1.7 ± 0.5 nM at 30 mM Mg^{2+} (Figure 3B). The mean and standard deviation values were calculated using data from three trials for each experimental condition (Supplementary

Figure S3). Results from these MST experiments show that binding of the Cy5–oligo to the 5′-extension was unaffected by changes in either Mg^{2+} concentration or reconstitution with RPPs.

We next determined the pre-tRNA cleavage activity of doubly fluor-labeled *Pfu* RPR ext mP1. At 450 mM Mg^{2+} and 37°C, cleavage of *Tth* pre-tRNA^{Gly} by Cy5–*Pfu* RPR ext mP1 + Cy3–oligo was ~5-fold lower than that of the unlabeled *Pfu* RPR ext mP1; we observed a ~3.3-fold decrease when we tested cleavage of *Eco* pre-tRNA^{Tyr} by the holoenzyme assembled with Cy5-labeled RPR ext mP1 relative to the unlabeled counterpart (Supplementary Table S4; see *Supplementary Information* for additional details). Because the doubly fluor-labeled RPR was functional, albeit less active than the unmodified counterpart, we proceeded with the ensemble FRET experiments. The loss of activity that we observed with the fluor-labeled RPR is not surprising and has precedents. For example, two different Cy3– and Cy5–dual labeled guide RNAs that were individually assembled into a H/ACA snoRNP and used in single-molecule fluorescence studies displayed 4- to 6-fold lower pseudouridylation activity relative to the unlabeled counterpart (11).

Activity and ensemble FRET assays using *Pfu* RPR ext mP1

Cleavage of 5′-[^{32}P]-pre-tRNA^{Gly} (120 µM) was assayed between 100 mM and 500 mM Mg^{2+}, and monitored by denaturing PAGE (Figure 4A, Supplementary Figure S4); all experiments were performed at 37°C (see *Supplementary Information* for the rationale underlying choice of 37°C). RPR activity was weak at 100 mM Mg^{2+} but the activity increased nearly 70-fold when [Mg^{2+}] was increased from 100 to 350 mM before plateauing (Figure 4B). A similar Mg^{2+}-dependent activity profile was also observed with *Eco* pre-tRNA^{Tyr}, a second substrate that we tested [Supplementary Figure S5 (25)].

FRET was measured from 10 mM to 500 mM Mg^{2+} and at 37°C in the same buffers used for activity assays. Upon excitation of the Cy3 donor, Cy5 emission was observed with the doubly labeled *Pfu* RPR ext mP1 thus confirming FRET (Figure 4C and Supplementary Figure S6). Mirroring the [Mg^{2+}]-dependent trend observed for turnover number, the FRET efficiency (E_{FRET}) also showed a gradual increase with increasing [Mg^{2+}], plateauing at 350–400 mM Mg^{2+} coinciding with the concentration where we observed maximal activity (see overlay in Figure 4D). These coincident trends highlight how FRET—a proxy for distance and contacts between the C and S domains—accurately tracks pre-tRNA cleavage. The increase in E_{FRET} values from 0.03 ± 0.01 at 10 mM to 0.20 ± 0.03 at 450 mM Mg^{2+} indicates a shift from an 'open' to a 'closed' conformation (Figure 6A, Scheme I).

Our finding of moderate E_{FRET} in 100–200 mM Mg^{2+}, where the RPR is weakly active, suggests that less Mg^{2+} is required for formation of tertiary structure compared to function (Figure 4). It is possible that diffusely-bound Mg^{2+} ions promote RPR tertiary structure, which in turn is required for occupancy of site-specific Mg^{2+} in the active site.
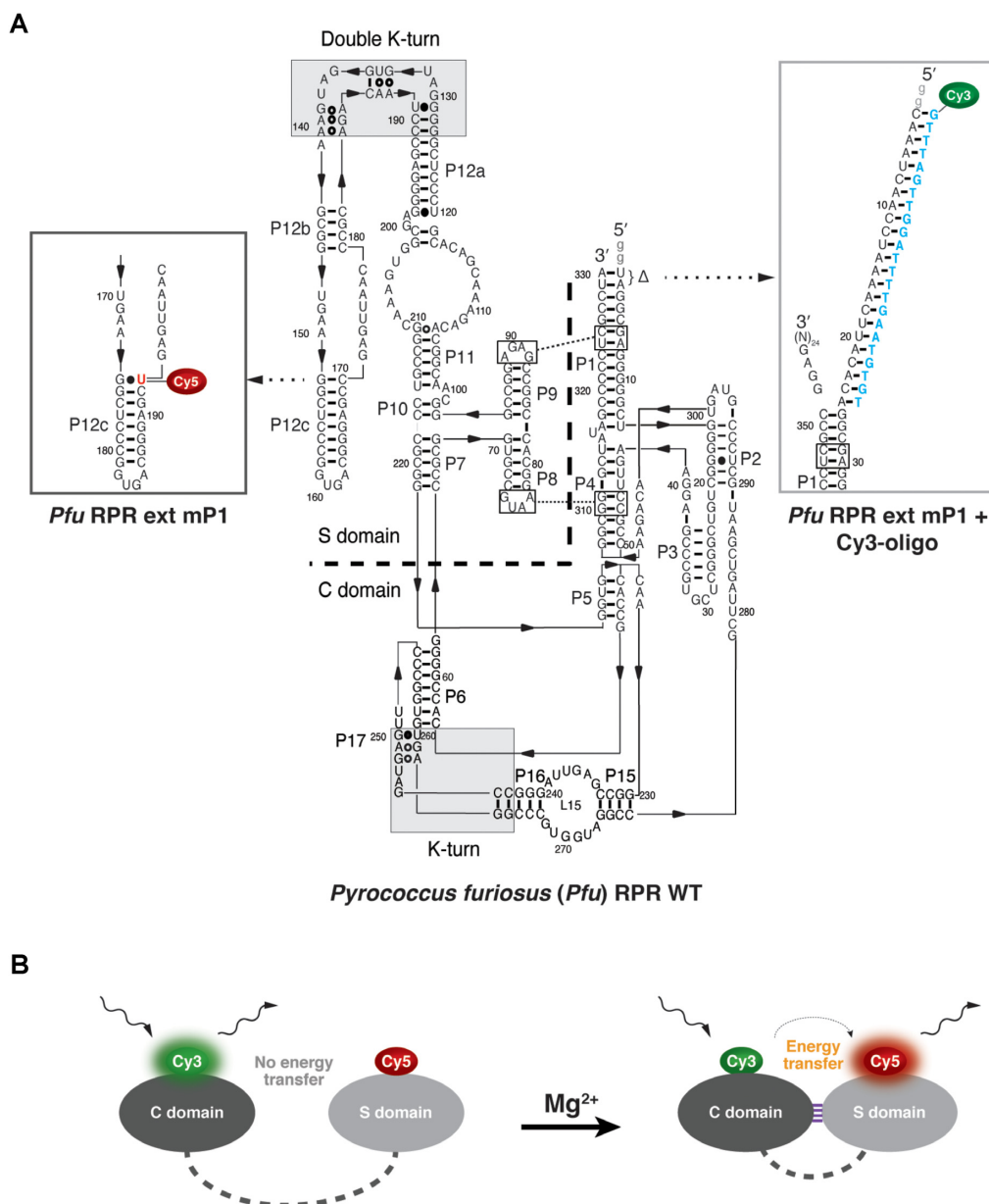
Figure 1. (**A**) A modified *Pyrococcus furiosus* RNase P RNA (*Pfu* RPR ext mP1) labeled with both Cy3 and Cy5 fluorophores. To generate *Pfu* RPR ext mP1, both the 5′- and 3′-termini were extended (inset, right) while the two terminal bp in the P1 helix were deleted. The cytidine at position 170 (wild-type numbering) was replaced with an amine-modified uridine (red) to facilitate internal Cy5 labeling via splint ligation (see Figure 2), and a Cy3-labeled DNA oligonucleotide was annealed to the 5′-end to obtain a dual-labeled RPR. (**B**) General scheme for Förster resonance energy transfer (FRET) studies. Increasing [Mg²⁺] is expected to promote interactions between the C (dark gray) and S (light gray) domains, thereby increasing the proximity of the Cy3 (donor) and Cy5 (acceptor) fluorophores and FRET efficiency.

Activity and ensemble FRET assays using the *Pfu* RNase P holoenzyme

To understand the effect of all five cognate RPPs on Mg²⁺-induced structural and functional changes in the RPR, we tested the activity of the RPR + 5 RPPs (POP5•RPP30, RPP21•RPP29, L7Ae) complex. Previous assays of *Pfu* RNase P at 55°C (7,50) informed the range of Mg²⁺ concentrations to be tested. The RPR + 5 RPP complex is active at 10 mM Mg²⁺ and 55°C. However, as our experiments were performed at 37°C, we explored a slightly wider range of Mg²⁺ concentrations (33 μM to 30 mM Mg²⁺) to

account for a possible temperature-dependent shift in the [Mg²⁺] that is optimal for activity. As the POP5•RPP30 and RPP21•RPP29 complexes are stored in Mg²⁺ (50), the lowest possible [Mg²⁺] we could test was ∼33 μM.

When cleavage of *Eco* pre-tRNA$^{\text{Tyr}}$ was analyzed by denaturing PAGE (Figure 5A), we observed activity starting at 1 mM Mg²⁺ (Figure 5B). As noticed with RPR alone, the holoenzyme showed a gradual increase in activity with increasing [Mg²⁺] and eventually plateaued at 20 mM (Figure 5B). The activity increased 42-fold as the [Mg²⁺] increased from 1 to 20 mM. While the actual turnover numbers with
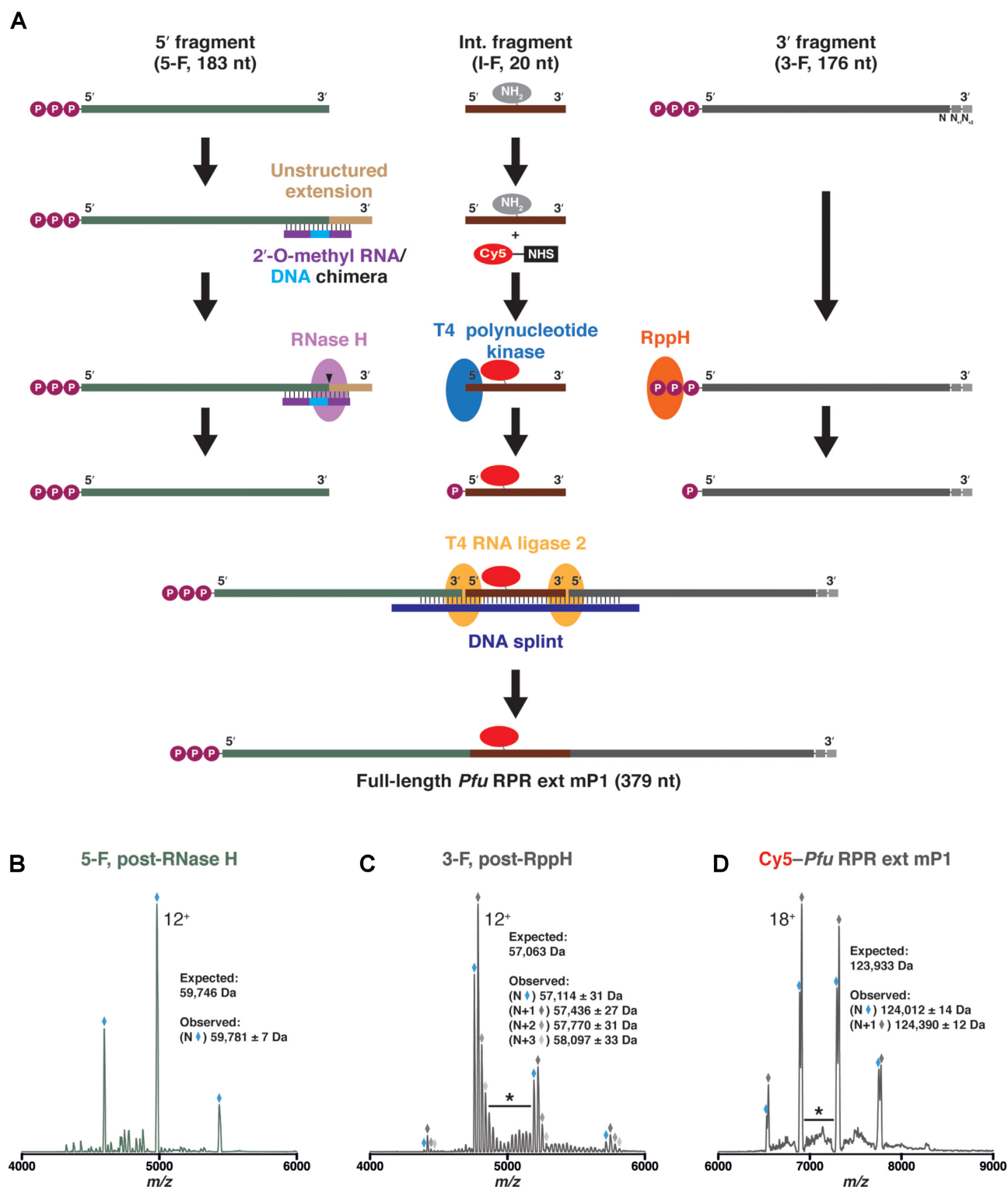
Figure 2. Use of splint ligation to internally label *Pfu* RPR ext mP1 with a Cy5 fluorophore. (**A**) The RPR was synthesized in three fragments: 5′-fragment (5-F, transcribed *in vitro*), internal fragment (I-F, commercially synthesized), and 3′-fragment (3-F, transcribed *in vitro*). Each fragment was processed individually prior to a two-step ligation using T4 RNA ligase 2 and a DNA splint. Mass spectrometry was used to verify the masses of the (**B**) 5′ fragment [5-F], post-RNase H cleavage; (**C**) 3′ fragment [3-F], post-RppH treatment; and (**D**) final *Pfu* RPR ext mP1 labeled with Cy5. Charge state distributions for the most intense species in each sample are indicated with diamonds, and the main charge state is labeled. In each spectrum, the species of intended length (N) is shown in blue while any prominent, 3′-extended species (N+#) are marked in varying shades of gray. Representative regions of low-intensity peaks that are indicative of additional heterogeneity have been denoted with an asterisk. In all spectra, the y-axis (not shown) represents relative intensity.
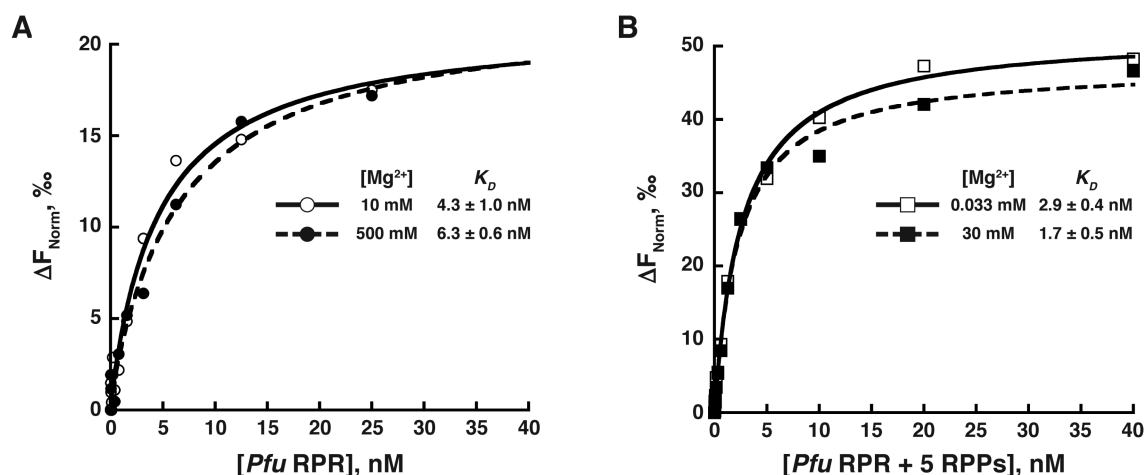
Figure 3. Representative microscale thermophoresis (MST) measurements of Cy5-labeled oligonucleotide (Cy5–oligo) binding to (**A**) unlabeled *Pfu* RPR ext mP1 at 10 mM (○, solid line) and 500 mM (●, dashed line) Mg^{2+}, and (**B**) *Pfu* RPR ext mP1 + 5 RPPs at 0.033 mM (□, solid line) and 30 mM (■, dashed line) Mg^{2+}. Plots were fit to a hyperbolic binding isotherm to yield K_D values. In the inset tables, mean and standard deviation values were calculated from three technical replicates (see Supplementary Figure S3 for the primary data from individual trials).
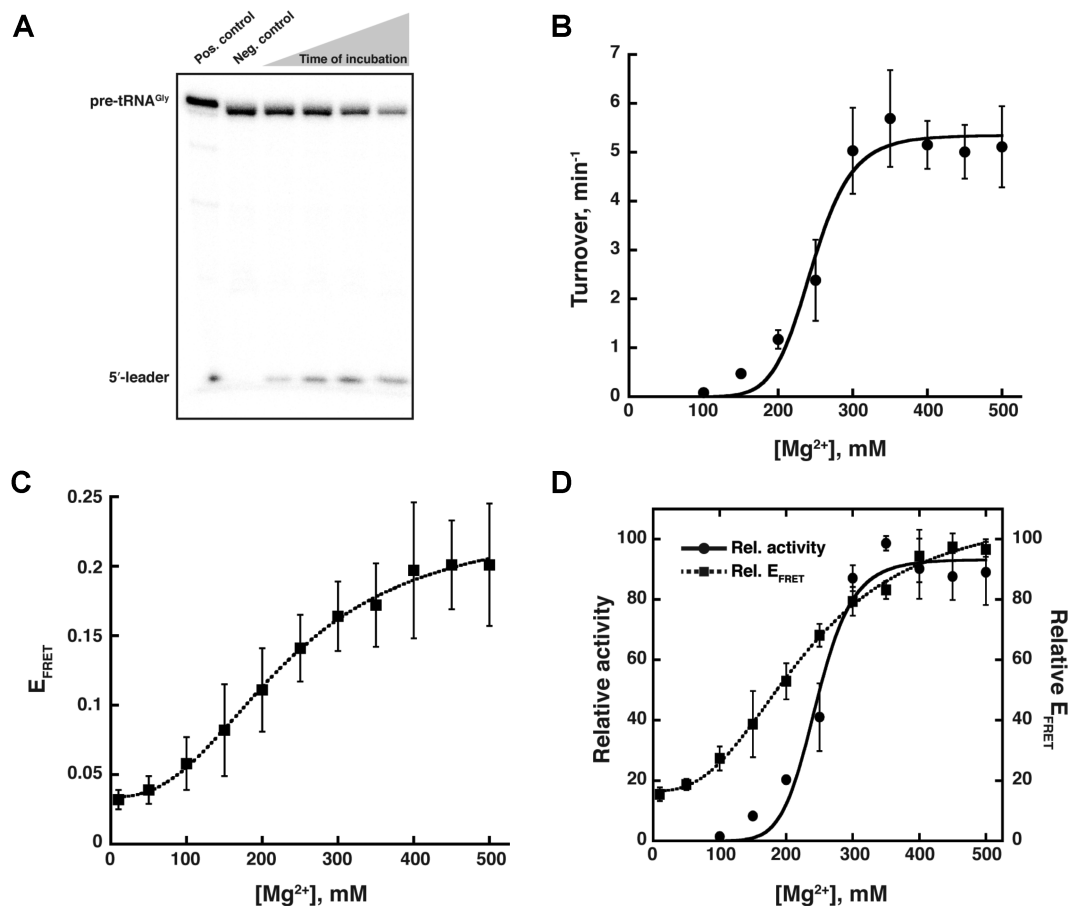
Figure 4. Effect of Mg^{2+} on the activity and inter-domain interactions of *Pfu* RPR ext mP1. (**A**) Representative data showing cleavage of γ-^{32}P-ATP-labeled *Thermus thermophilus* (*Tth*) pre-tRNA^{Gly} by unlabeled *Pfu* RPR ext mP1 in 450 mM Mg^{2+} and at 37°C during a 20-min time-course (also, see Supplementary Figure S4 and S5). (**B**) Mg^{2+}-dependent increase in the activity of unlabeled *Pfu* RPR ext mP1. Average turnover numbers calculated from four independent initial velocity measurements are plotted against [Mg^{2+}]. (**C**) Mg^{2+}-dependent increase in FRET efficiency for dual-fluor-labeled *Pfu* RPR ext mP1. Average FRET efficiencies obtained from three independent measurements are plotted against [Mg^{2+}] (see Supplementary Figure S6 for additional data). (**D**) Overlay of turnover number (solid line) and FRET efficiency (dashed line), which shows that FRET efficiency correlates with the rate of catalysis as a function of [Mg^{2+}]. Relative activity and E$_{FRET}$ values were obtained by normalization against the highest turnover number or FRET efficiency, respectively; since this reference value was not always at the same concentration of Mg^{2+} among the replicates, there is minor variability between panels B or C versus D but the trends are highly similar. In instances where error bars are not seen, the errors are smaller than the symbols used.
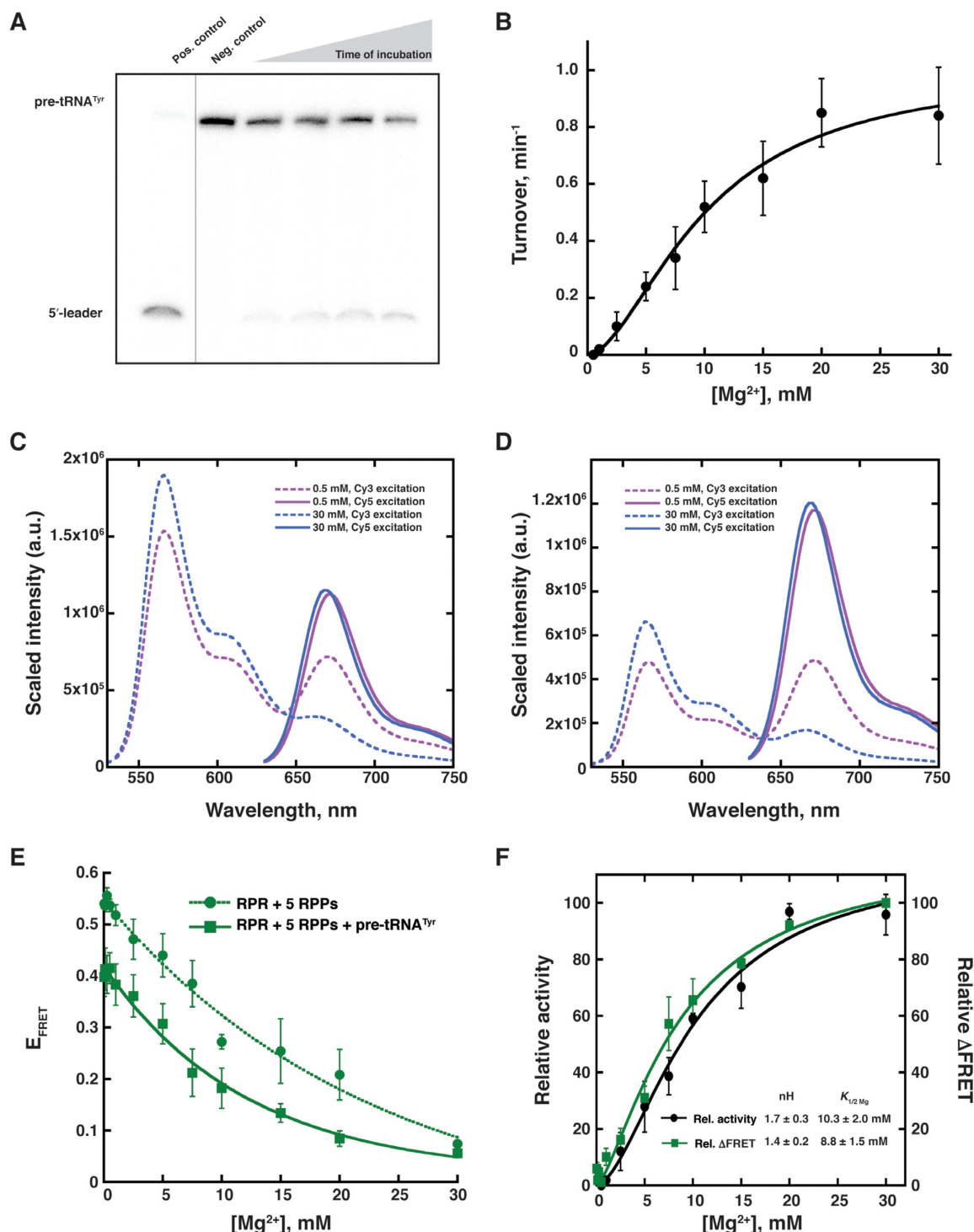
Figure 5. Effect of Mg^{2+} on the activity and inter-domain interactions of *Pfu* RPR ext mP1 reconstituted with all 5 RPPs. (**A**) Representative data showing cleavage of γ-^{32}P-ATP-labeled *Escherichia coli* (*Eco*) pre-tRNA^{Tyr} by unlabeled *Pfu* RPR ext mP1 + 5 RPPs in 30 mM Mg^{2+} and at 37°C during a 5-min time-course. For illustrative purposes, the gel was cropped to reposition non-adjacent lanes of interest; no other modifications were made to the image. (**B**) Mg^{2+}-dependent increase in the activity of unlabeled *Pfu* RPR ext mP1. Average turnover numbers calculated from three independent initial velocity measurements are plotted against [Mg^{2+}], and the data were fit to the Hill equation. Dual-fluor-labeled *Pfu* RPR ext mP1 + 5 RPPs (**C**) without and (**D**) with *Eco* pre-tRNA^{Tyr} shows a decrease in FRET from low (0.5 mM; purple) to high (30 mM; red) Mg^{2+}. A representative spectrum from one trial at each Mg^{2+} concentration is shown. Within each set, emission from direct Cy5 excitation was normalized against the sample with the highest signal. The same scaling factor was then applied to the corresponding emission spectrum obtained from Cy3 excitation (see Supplementary Figure S10 for additional data). (**E**) Mg^{2+}-dependent increase in FRET efficiency for dual-fluor-labeled *Pfu* RPR ext mP1 + 5 RPPs without (dotted line) and with (solid line) *Eco* pre-tRNA^{Tyr}. Average FRET efficiency from three independent measurements is plotted against [Mg^{2+}]. (**F**) Comparison of relative turnover numbers (black) and ΔFRET values (green solid line). Data for *Pfu* RPR ext mP1 + 5 RPPs + *Eco* pre-tRNA^{Tyr} were fit to the Hill equation to obtain the n_H (Hill coefficient) and $K_{1/2}Mg^{2+}$ values in the inset (see Supplementary Figure S11 for additional data).

the RPR + 5 RPP complex were lower than that observed with the RPR alone (Figures 4 and 5), these assays entailed use of different substrates and assay conditions; also, note that the range of Mg^{2+} concentrations tested for the RPR and holoenzyme are quite different (Supplementary Figure S7).

Although we used a stochiometric excess of RPPs to promote assembly of the *Pfu* RNase P holoenzyme and had some previous evidence from native MS for assembly of the RNP at low Mg^{2+} (7,51), we used two approaches to test the idea that the complete holoenzyme (RPR + all five RPPs) is assembled at very low and high $[Mg^{2+}]$. First, to investigate if the activity observed with RPR + 5 RPPs could have resulted from partial assemblies, we performed pre-tRNA^{Tyr} cleavage assays using RPR assembled with either RPP21•RPP29 + POP5•RPP30 or POP5•RPP30 + L7Ae. Of these two combinations, RPR + POP5•RPP30 + L7Ae was more active under the assay conditions tested but even this 3-RPP complex fared weaker than the 5-RPP complex between 1 and 15 mM Mg^{2+} (Supplementary Figure S8). Thus, activity at <15 mM Mg^{2+} is attributable to a complex containing 5 RPPs. Second, we assessed *Pfu* RNase P assembly using mass photometry (MP), a powerful tool to gain information on the oligomeric state of proteins either alone or in complexes (71,72). Despite being of lower mass accuracy than native MS, MP has the advantage of permitting measurements in non-volatile salts such as those typically used in assay buffers (e.g., Mg^{2+}, HEPES). When we examined the *Pfu* RPR ± 5 RPPs at 33 μM and 10 mM Mg^{2+}, we observed a mass range consistent with the RPR assembled into a complex with 5 RPPs (RPR + POP5•RPP30 + RPP21•RPP29 + L7Ae$_3$; Supplementary Figure S9). However, the broad MP profiles also make it difficult to determine if the RPR is fully assembled into a stable RNP containing all five RPPs. The RPR and RPPs may be in dynamic equilibrium at low Mg^{2+}, and increasing Mg^{2+} could enhance both the binding affinity of the RPPs (e.g. third copy of L7Ae; (7)) and the stability of the holoenzyme on account of gains in RPR and RPP co-folding. Nevertheless, it appears that the complete holoenzyme is assembled at very low and high $[Mg^{2+}]$.

The RPR was reconstituted with the 5 RPPs, and FRET was measured at 37°C. Surprisingly, unlike the RPR alone, the holoenzyme was associated with an $E_{FRET} = 0.54 \pm 0.02$ even at 33 μM Mg^{2+}. Contrary to the trend observed with RPR alone, there was a decrease in the holoenzyme's E_{FRET} with increasing $[Mg^{2+}]$, with a two-fold drop to 0.25 ± 0.06 at 15 mM Mg^{2+} (Figure 5C, E and Supplementary Figure S10). This finding leads to three inferences. First, the Mg^{2+}-dependent self-organization in the holoenzyme is complete at much lower Mg^{2+} concentrations compared to the RPR alone (20 mM versus 400 mM; Figures 4D and 5E). Second, increasing $[Mg^{2+}]$ leads to an increase in distance between Cy3 and Cy5 in case of the holoenzyme, which contrasts sharply with the observed decrease in the case of RPR alone (Figures 4D and 5E). The gradual Mg^{2+}-dependent decrease in E_{FRET} observed with RPR + 5 RPPs might reflect Mg^{2+}-induced remodeling of the RNP complex and suggests a shift from a 'constrained' to a 'closed (not collapsed)' conformation (Figure 6B, Scheme I). We recog-

nize that other perspectives merit consideration since not all RNAs undergo protein-induced structural remodeling ((4); see Discussion). Lastly, similar E_{FRET} values for the RPR without or with 5 RPPs at the Mg^{2+} concentration where their activities begin to plateau suggests that they each take a different path to reach a similar conformation that is optimal for catalysis.

The E_{FRET} values for the RPR and holoenzyme, respectively, of 0.03 and 0.54 (at 33 μM Mg^{2+}) prompted us to determine if this difference might arise from RPPs inducing changes in the local environment of the fluorophore and not by altering the RPR structure. When the RPR was assembled as part of sub-complexes (with POP5•RPP30 or RPP21•RPP29 + L7Ae), we obtained E_{FRET} ~0.4 to 0.45 in the presence of 33 μM Mg^{2+}. Given the possibility of a 'collapsed-state' ensemble even in the sub-assemblies, it seems unlikely that the large FRET changes observed with the RPR + 5 RPPs would arise from perturbations to the local environment of the fluor especially with two suites of RPPs with different physicochemical properties. Also, protein-induced fluorescence enhancement typically results in ~2- to 3-fold gains unlike what we observed.

Ensemble FRET measurements with *Pfu* RPR ext mP1 + 5 RPPs + pre-tRNA^{Tyr}

We employed FRET to gain insights into the conformational changes in the holoenzyme in the presence of pre-tRNA^{Tyr} (Figure 5D). We do not expect more than one percent of the substrate to be cleaved during the three-min period of each FRET measurement given the turnover number of the Cy5 *Pfu* RPR ext mP1 (Supplementary Table S4). As pre-tRNA^{Tyr} is present in 20-fold excess over the holoenzyme, changes in FRET efficiency as a function of increasing $[Mg^{2+}]$ are therefore likely to reflect structural alterations in the enzyme-substrate (ES) complex. When FRET was measured in the presence of pre-tRNA^{Tyr}, we observed a trend similar to that observed with the holoenzyme alone (Figure 5E, solid vs dotted lines). However, we extracted an important feature from these data by plotting the relative change in E_{FRET}. We calculated $\Delta FRET = (Max_{FRET} - E_{FRET})/(Max_{FRET} - Min_{FRET}) \times 100$ at each $[Mg^{2+}]$ tested. When either the turnover numbers or $\Delta FRET$ values were plotted as a function of Mg^{2+} (Figure 5F), they could be fit to the Hill equation and there was good agreement in the n_H (Hill coefficient, 1.7 ± 0.3 or 1.4 ± 0.2, respectively) and $K_{1/2}^{Mg^{2+}}$ (10.3 ± 2.0 and 8.8 ± 1.5 mM, respectively). These values indicate that at least two Mg^{2+} ions bind cooperatively, although the second ion might be bound weakly/transiently.

Since the abovementioned cooperativity is absent when we examined $\Delta FRET$ of the RPR + 5 RPP complex alone (Figure 5E, Supplementary Figure S11), substrate binding is associated with this cooperativity. However, we investigated if one assay variable might have contributed to the observed difference. We had used the Cy3–oligo at a two-fold excess over the RPR in case of the holoenzyme and a slightly sub-stoichiometric amount with the holoenzyme–substrate assays (see *Materials and Methods*) since we were concerned about potential non-specific binding of the Cy3–oligo to
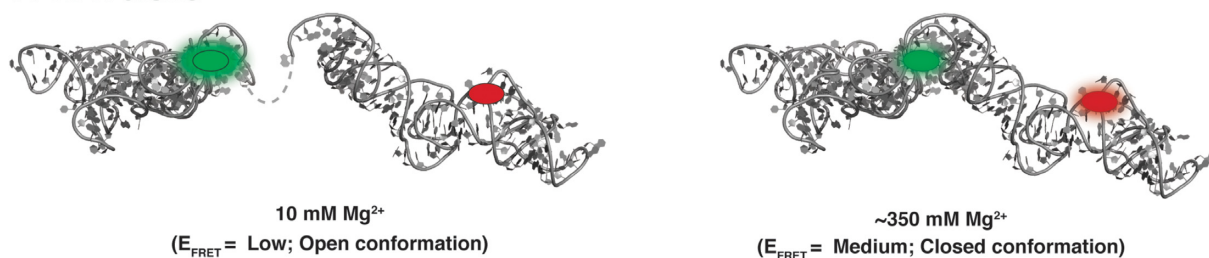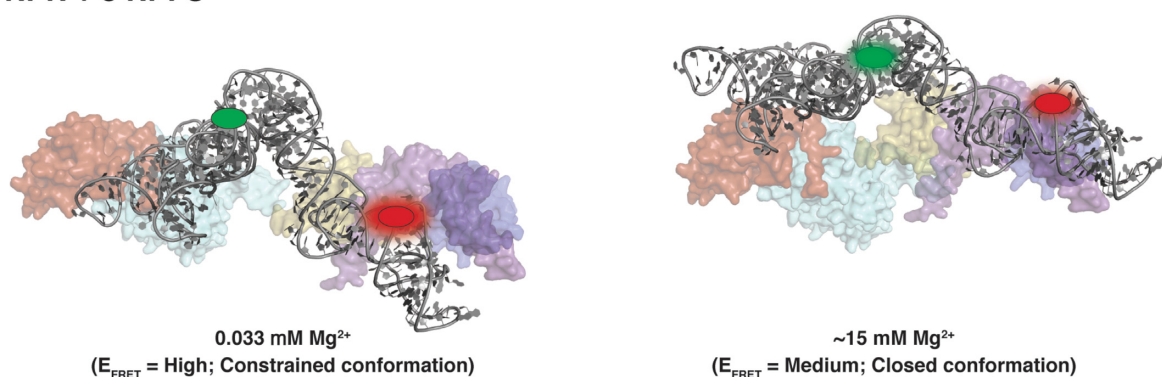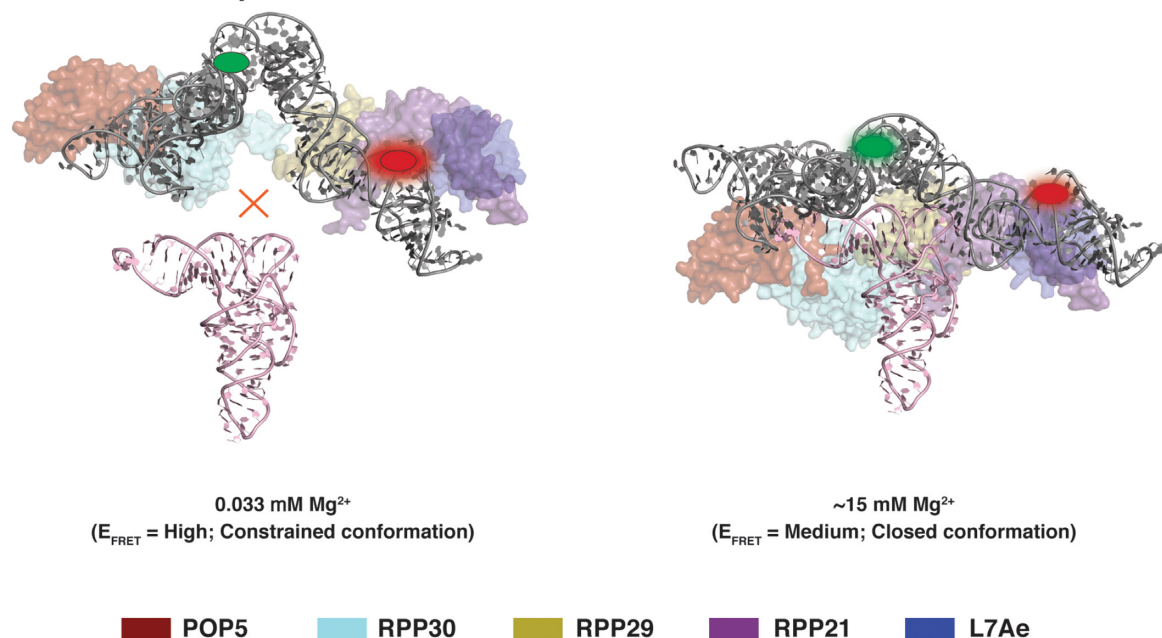
Figure 6. Model of potential structural changes in archaeal RNase P (also, see Scheme I). Based on the ensemble FRET measurements, the RPR (gray) alone likely adopts an 'open' conformation (low FRET efficiency; **A**, left) at 10 mM Mg^{2+} while the complex of *Pfu* RPR + 5 RPPs exists in a 'constrained' conformation (high FRET efficiency; **B**, left) at 0.033 mM Mg^{2+}. Neither state is competent for pre-tRNA cleavage (**C**, left). With increasing [Mg^{2+}], both the RPR and the holoenzyme complex comprised of *Pfu* RPR + 5 RPPs undergo structural remodeling to converge on a common 'closed' active conformation (**A**–**C**, right). While there are caveats to using ensemble FRET measurements to establish a precise distance between two fluorophores, conservation of the active site and pre-tRNA anchors in different RNase P RNP variants provide some support for this qualitative model generated using the cryo-EM structure of *Methanocaldococcus jannaschii* (*Mja*) RNase P as template (40). Although we depict single conformations in this model for the sake of simplicity, each state is more accurately described by an ensemble. E_{FRET} classified using $0.03 < low < 0.10 < medium < 0.30 < high < 0.60$.

the excess pre-tRNA. Nevertheless, when we compared E_{FRET} and the Hill equation curve-fits for the holoenzyme-substrate complex using either the two-fold excess or the sub-stoichiometric amount of the Cy3–oligo, the Hill coefficient and $K_{1/2}^{Mg2+}$ values were similar (n_H = 1.4 or 1.5; $K_{1/2}^{Mg2+}$ 8.8 or 5.6 mM; Supplementary Figure S11). Thus, the difference that we observed between the holoenzyme and holoenzyme–substrate complex (Figure 5E and Supplementary Figure S11) with respect to Mg^{2+} cooperativity is due to substrate binding.

DISCUSSION

We elaborate below the implications of four findings from our study of *Pfu* RNase P: (i) FRET monitored using Cy3-$RPR_{C domain}$ and Cy5-$RPR_{S domain}$ correlates well with pre-tRNA cleavage activity; (ii) the RPR and the holoenzyme (RPR + 5 RPPs) traverse different Mg^{2+}-dependent paths to converge on similar functional states (Figure 6); (iii) the *Pfu* RNase P holoenzyme (RPR + 5 RPPs) is remodeled by increasing Mg^{2+}; and (iv) binding of the pre-tRNA substrate to the holoenzyme influences the cooperativity of Mg^{2+} binding and catalysis.

Interdomain interactions in *Pfu* RPR are essential for catalysis

The bacterial, archaeal, and eukaryotic RNase P holoenzyme-tRNA structures reveal the invariant use of a shallow pocket to bind the acceptor–T arm in the substrate (Supplementary Figure S1C and D) (38–41). In all three cases, cleavage between N_{-1} and N_{+1} in the pre-tRNA substrate depends on at least two specific contacts: the G_{19}–C_{56} base pair (bp) of the tRNA elbow that forms π-π interactions with two interdigitated T loops in the RPR's S domain, and the first bp of the acceptor stem ($N_{+1} - N_{+72}$) that is recognized by the RPR's C domain through either RNA or RNP contacts (38–41). If this dual anchor is used as a molecular ruler to trigger site-specific cleavage, optimal substrate recognition must require the C and S domains to interact and be oriented appropriately with respect to each other. Such a postulate, first inspired by biochemical and phylogenetic studies of bacterial RNase P (43,44,73), is applicable to *Pfu* RNase P. *Pfu* RPR displays optimal activity in 300–400 mM Mg^{2+}, while the RPR + 5 RPP complex activity starts to plateau around 15–20 mM Mg^{2+} (Figures 4 and 5). The coincident E_{FRET} values (0.15–0.25) at these optimal [Mg^{2+}] suggests that a specific RPR conformation is required for pre-tRNA cleavage.

RPR and the holoenzyme achieve a common functional fold albeit through different paths

Even though the RPR conformation either alone or in the holoenzyme has a different 'starting line', it reaches a similar final destination albeit through different routes. The parallel Mg^{2+}-dependent increase in E_{FRET} and activity (Figure 4) for the *Pfu* RPR alone suggests that decreasing the distance between the C (Cy3) and S (Cy5) domains is associated with an increase in turnover number. The low E_{FRET} at 10 mM Mg^{2+} is indicative of an RPR_{Open} conformation; this

state transitions to a medium E_{FRET} conformation at 300–400 mM Mg^{2+} where the RPR is active (RPR_{Closed}; Figure 6A; Scheme I). Clearly, both conformations are thermodynamically stable. Compared to the RPR, the high E_{FRET} observed with the holoenzyme at <1 mM Mg^{2+} suggests the presence of an $RNP_{Constrained}$ conformation that is not functional. Increasing [Mg^{2+}] from <1 to 15 mM results in the holoenzyme adopting a medium E_{FRET} and active conformation (RNP_{Closed}; Figure 6B and C, Scheme I). Thus, the RPR and the holoenzyme converge on similar final state(s) but after traversing different paths.
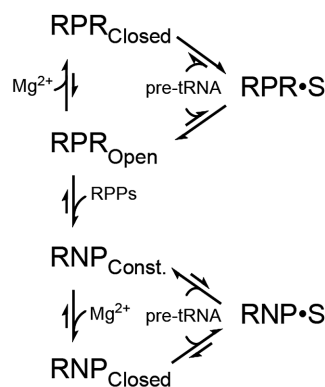
Scheme I

Mg^{2+}-induced remodeling of the RNase P RNP

The E_{FRET} values for the RPR and holoenzyme, respectively, are 0.03 and 0.54 (at 33 μM Mg^{2+}) and 0.03 and 0.27 (at 10 mM Mg^{2+}) (Figure 5; data not shown). These unexpected differences in E_{FRET} values indicate that the RPR is present in two distinct conformational ensembles, one when alone and the other as part of the holoenzyme. Comparison of the bacterial RPR without and with its single RPP showed minimal changes in the RPR structure (38). Since there is no structure available for the archaeal or eukaryotic RPR alone, their remodeling (if any) upon binding to their cognate RPPs is unknown. However, MD simulations of the yeast RPR and holoenzyme (RPR + 9 RPPs) showed large fluctuations in the RPR backbone that increased the distance between the two structural elements needed for dual anchoring of the pre-tRNA substrate (39). Addition of the RPPs constrained the RPR's dynamic behavior except in two regions that do not bind the RPPs (39). These MD simulations and our FRET studies suggest that the archaeal (and possibly eukaryotic) RPRs in the absence or presence of RPPs might sample a different conformational ensemble, perhaps allowing regulatory control of the holoenzyme not possible with the lone RPR.

The Mg^{2+}-dependent decrease in E_{FRET} and increased pre-tRNA cleavage observed with the holoenzyme (Figure 5) is consistent with a few not mutually exclusive conclusions. First, while the bacterial RPR forms three long-range, inter-domain interactions—L9-P1, L8-P4 and L18-P8 (38,45)—the archaeal and eukaryotic RPRs have only the L9-P1 contact and instead use RPPs as scaffolds to stabilize the final fold (39–41). The cryo-EM structure of *Mja* (archaeal) RNase P (40) illustrates how this scaf-

folding is made possible by stringing together five RPPs through protein-protein interactions. However, rather than a static structure, our data support the idea of Mg^{2+}-induced distortion/wedging to rearrange the RPPs and convert the holoenzyme from a 'constrained' to a 'closed (but less collapsed)' conformation (Figure 6B, Scheme I). A similar strain-propagation model was proposed based on SHAPE studies of the bI5 group I intron with and without its two protein cofactors (2). Second, if Mg^{2+} and RPPs bind to the RPR in its folded state, their binding will be thermodynamically coupled and cause remodeling of the RNase P RNP. With FRET as an output, we plan to test this premise. Ongoing single-molecule FRET studies will also help determine the population distribution of different sub-assemblies and the effect of partial suites of RPPs on RPR structural conformations. We expect to map the hierarchy and cooperativity among RPPs during RNase P assembly and determine the contribution of such linkages to activity over a range of $[Mg^{2+}]$. Such experiments have been instructive in revealing RNA structural dynamics and the temporal order of protein-binding events in telomerase, U4/U6 di-snRNP, and the H/ACA snoRNP (4,11,13).

We highlight some similarities and differences between our findings and previous studies that examined RNA folding and RNP assembly. First, ensemble and single-molecule FRET studies show that Na^+ and Mg^{2+} are capable of promoting 'closed' RNA conformations by decreasing the rate of unfolding of the folded state (6,65). Mg^{2+} acts likewise in the case of *Pfu* RPR alone, although $E_{FRET} = 0.03$ at 2 M NH_4^+ (in low Mg^{2+}) suggests that offsetting the electrostatic repulsion by screening alone is insufficient (Figure 4C) and that Mg^{2+} is necessary to promote inter-domain interactions associated with a functional fold. Second, results from investigations of small RNPs or isolated modules of larger RNPs show how proteins can alter the equilibrium between an open and docked/closed state and outperform Mg^{2+} alone in influencing this conformational toggling. Steady-state FRET measurements revealed that L7Ae can bind an RNA containing a kink-turn even in the absence of metal ions and promote a kinked conformation that is observed with Mg^{2+} alone; a small increase in E_{FRET} in the presence of L7Ae and Mg^{2+} (compared to either alone) suggests additional protein binding-mediated stabilization (15). Results from ensemble FRET and footprinting experiments with the *Eco* 16S rRNA 5′ domain showed that the native conformation (albeit not fully populated) is achieved by 10 mM Mg^{2+}. At 4 mM Mg^{2+}, however, S4 along with S16 and S20, which act cooperatively on the RNA either by stabilizing the native or destabilizing the non-native state, are necessary for rRNA folding (18). SMF studies with a yeast U2 snRNA model showed that either Mg^{2+} or the Cus2p protein stabilize the 'open' conformation required for catalysis rather than the 'closed' conformation needed for assembly (10). However, Mg^{2+} and Cus2p together also resulted in less frequent sampling of certain conformations promoted by Mg^{2+} alone. The decreased FRET with increased Mg^{2+} in the Cus2p-U2 snRNA complex mirrors the trend that we observed with *Pfu* RNase P (Figure 5E). These two cases show how Mg^{2+} and proteins engender a concerted distortion to transition the RNP from a compact assembly to an extended functional state. There is a key dif-

ference, however, between *Pfu* RNase P and other RNPs studied thus far. Typically, protein cofactors shift the equilibrium between pre-existing conformational ensembles of their respective RNA ligand. The high E_{FRET} (∼0.5) of the *Pfu* RNase P holoenzyme that is not observed with the RPR alone suggests a new collapsed RPR conformation but the inability to parse heterogeneity in ensemble experiments precludes firm conclusions in this regard. Since ensemble averages mask the proportion of sub-populations, rare conformations (including those with high E_{FRET}) in the RPR-alone sample will not be evident.

Coupling between induced fit and Mg^{2+} coordination

There appear to be no dramatic alterations in the structure of the holoenzyme upon binding to the substrate as judged by the similar FRET profiles (Figure 5E). This claim is consistent with the cryo-EM structures of *Mja* RNase P (40) that show little difference in the overall architecture of the RPR and RPPs in the absence or presence of $tRNA^{Tyr}$. However, we found cooperativity in the Mg^{2+} response when the substrate is present. One interpretation of these findings is that the substrate participates in shaping the active site, perhaps even bringing with it a Mg^{2+} (74). Moreover, since bacterial RPR S-domain mutants that are incapable of reading the tRNA 'elbow' could be rescued by increasing Mg^{2+} (57,60), it appears that interdomain crosstalk leads to a rearrangement of Mg^{2+} in the active site. Our FRET studies confirm the interplay between the induced fit triggered by substrate binding and positioning of catalytically relevant metal ions. FRET studies with 'elbow-lacking' model substrates that cannot engender inter-domain signaling would provide further support for this notion of Mg^{2+} coordination that is associated with induced fit.

SUMMARY

The retention of RNA enzymes in the extant cellular pool of protein-based catalysts has been attributed to their ability to leverage substrate binding to effect long-range induced fit and efficiently sample conformational ensembles (75). Such gating mechanisms afford exquisite control of rate and fidelity, not unlike protein-only enzymes (76). Under low-Mg^{2+} cellular conditions, however, such regulation in catalytic RNAs may depend on proteins as exemplified by RPPs that fasten distal RPR structural elements to facilitate pre-tRNA recognition and local Mg^{2+}-interaction networks essential for catalysis. Our finding that proteins may promote new RNA conformational ensembles that can be fine-tuned differently by cellular Mg^{2+} supports the notion that functional and regulatory gains shaped the evolutionary forces that favored a functional alliance between RNA and protein in essential cellular RNPs.

SUPPLEMENTARY DATA

Supplementary Data are available at NAR Online.

ACKNOWLEDGEMENTS

REFERENCES

1. Bokinsky,G., Nivon,L.G., Liu,S., Chai,G., Hong,M., Weeks,K.M. and Zhuang,X. (2006) Two distinct binding modes of a protein cofactor with its target RNA. *J. Mol. Biol.*, **361**, 771–784.
2. Duncan,C.D. and Weeks,K.M. (2010) Nonhierarchical ribonucleoprotein assembly suggests a strain-propagation model for protein-facilitated RNA folding. *Biochemistry*, **49**, 5418–5425.
3. Froschauer,E.M., Kolisek,M., Dieterich,F., Schweigel,M. and Schweyen,R.J. (2004) Fluorescence measurements of free [Mg2+] by use of mag-fura 2 in Salmonella enterica. *FEMS Microbiol. Lett.*, **237**, 49–55.
4. Hardin,J.W., Warnasooriya,C., Kondo,Y., Nagai,K. and Rueda,D. (2015) Assembly and dynamics of the U4/U6 di-snRNP by single-molecule FRET. *Nucleic. Acids. Res.*, **43**, 10963–10974.
5. Kim,H., Abeysirigunawardena,S.C., Chen,K., Mayerle,M., Ragunathan,K., Luthey-Schulten,Z., Ha,T. and Woodson,S.A. (2014) Protein-guided RNA dynamics during early ribosome assembly. *Nature*, **506**, 334–338.
6. Kim,H.D., Nienhaus,G.U., Ha,T., Orr,J.W., Williamson,J.R. and Chu,S. (2002) Mg2+-dependent conformational change of RNA studied by fluorescence correlation and FRET on immobilized single molecules. *Proc. Natl Acad. Sci. U.S.A.*, **99**, 4284–4289.
7. Lai,L.B., Tanimoto,A., Lai,S.M., Chen,W.Y., Marathe,I.A., Westhof,E., Wysocki,V.H. and Gopalan,V. (2017) A novel double kink-turn module in euryarchaeal RNase P RNAs. *Nucleic Acids Res.*, **45**, 7432–7440.
8. Mayerle,M., Bellur,D.L. and Woodson,S.A. (2011) Slow formation of stable complexes during coincubation of minimal rRNA and ribosomal protein S4. *J. Mol. Biol.*, **412**, 453–465.
9. Pyle,A.M. (2002) Metal ions in the structure and function of RNA. *J. Biol. Inorg. Chem.*, **7**, 679–690.
10. Rodgers,M.L., Tretbar,U.S., Dehaven,A., Alwan,A.A., Luo,G., Mast,H.M. and Hoskins,A.A. (2016) Conformational dynamics of stem II of the U2 snRNA. *RNA*, **22**, 225–236.
11. Schmidt,A., Hanspach,G. and Hengesbach,M. (2020) Structural dynamics govern substrate recruitment and catalytic turnover in H/ACA RNP pseudouridylation. *RNA Biol.*, https://doi.org/10.1080/15476286.2020.1842984.
12. Schroeder,R., Barta,A. and Semrad,K. (2004) Strategies for RNA folding and assembly. *Nat. Rev. Mol. Cell Biol.*, **5**, 908–919.
13. Stone,M.D., Mihalusova,M., O'Connor,C.M., Prathapam,R., Collins,K. and Zhuang,X. (2007) Stepwise protein-mediated RNA folding directs assembly of telomerase ribonucleoprotein. *Nature*, **446**, 458–461.
14. Sun,L. and Harris,M.E. (2007) Evidence that binding of C5 protein to P RNA enhances ribozyme catalysis by influencing active site metal ion affinity. *RNA*, **13**, 1505–1515.
15. Turner,B., Melcher,S.E., Wilson,T.J., Norman,D.G. and Lilley,D.M. (2005) Induced fit of RNA on binding the L7Ae protein to the kink-turn motif. *RNA*, **11**, 1192–1200.
16. Weeks,K.M. and Cech,T.R. (1995) Protein facilitation of group I intron splicing by assembly of the catalytic core and the 5′ splice site domain. *Cell*, **82**, 221–230.
17. Yu,G., Zhao,Y. and Li,H. (2018) The multistructural forms of box C/D ribonucleoprotein particles. *RNA*, **24**, 1625–1633.
18. Abeysirigunawardena,S.C. and Woodson,S.A. (2015) Differential effects of ribosomal proteins and Mg2+ ions on a conformational switch during 30S ribosome 5′-domain assembly. *RNA*, **21**, 1859–1865.
19. Corley,M., Burns,M.C. and Yeo,G.W. (2020) How RNA-binding proteins interact with RNA: molecules and mechanisms. *Mol. Cell*, **78**, 9–29.
20. Hansen,S.R., Rodgers,M.L. and Hoskins,A.A. (2016) Fluorescent labeling of proteins in whole cell extracts for single-molecule imaging. *Methods Enzymol.*, **581**, 83–104.
21. Tamaru,D., Amikura,K., Shimizu,Y., Nierhaus,K.H. and Ueda,T. (2018) Reconstitution of 30S ribosomal subunits in vitro using ribosome biogenesis factors. *RNA*, **24**, 1512–1519.
22. Chen,W.Y., Pulukkunat,D.K., Cho,I.M., Tsai,H.Y. and Gopalan,V. (2010) Dissecting functional cooperation among protein subunits in archaeal RNase P, a catalytic ribonucleoprotein complex. *Nucleic Acids Res.*, **38**, 8316–8327.
23. Chen,W.Y., Singh,D., Lai,L.B., Stiffler,M.A., Lai,H.D., Foster,M.P. and Gopalan,V. (2012) Fidelity of tRNA 5′-maturation: a possible basis for the functional dependence of archaeal and eukaryal RNase P on multiple protein cofactors. *Nucleic Acids Res.*, **40**, 4666–4680.
24. Pulukkunat,D.K. and Gopalan,V. (2008) Studies on *Methanocaldococcus jannaschii* RNase P reveal insights into the roles of RNA and protein cofactors in RNase P catalysis. *Nucleic Acids Res.*, **36**, 4172–4180.
25. Tsai,H.Y., Pulukkunat,D.K., Woznick,W.K. and Gopalan,V. (2006) Functional reconstitution and characterization of Pyrococcus furiosus RNase P. *Proc. Natl Acad. Sci. U.S.A.*, **103**, 16147–16152.
26. Cho,I.M., Lai,L.B., Susanti,D., Mukhopadhyay,B. and Gopalan,V. (2010) Ribosomal protein L7Ae is a subunit of archaeal RNase P. *Proc. Natl Acad. Sci. U.S.A.*, **107**, 14573–14578.
27. Fukuhara,H., Kifusa,M., Watanabe,M., Terada,A., Honda,T., Numata,T., Kakuta,Y. and Kimura,M. (2006) A fifth protein subunit Ph1496p elevates the optimum temperature for the ribonuclease P activity from *Pyrococcus horikoshii* OT3. *Biochem. Biophys. Res. Commun.*, **343**, 956–964.
28. Perederina,A., Berezin,I. and Krasilnikov,A.S. (2018) In vitro reconstitution and analysis of eukaryotic RNase P RNPs. *Nucleic Acids Res.*, **46**, 6857–6868.
29. Kikovska,E., Svard,S.G. and Kirsebom,L.A. (2007) Eukaryotic RNase P RNA mediates cleavage in the absence of protein. *Proc. Natl Acad. Sci. U.S.A.*, **104**, 2062–2067.
30. Pannucci,J.A., Haas,E.S., Hall,T.A., Harris,J.K. and Brown,J.W. (1999) RNase P RNAs from some Archaea are catalytically active. *Proc. Natl Acad. Sci. U.S.A.*, **96**, 7803–7808.
31. Altman,S. (2007) A view of RNase P. *Mol. Biosyst.*, **3**, 604–607.
32. Ellis,J.C. and Brown,J.W. (2009) The RNase P family. *RNA Biol.*, **6**, 362–369.
33. Esakova,O. and Krasilnikov,A.S. (2010) Of proteins and RNA: the RNase P/MRP family. *RNA*, **16**, 1725–1747.

34. Evans,D., Marquez,S.M. and Pace,N.R. (2006) RNase P: interface of the RNA and protein worlds. *Trends Biochem. Sci.*, **31**, 333–341.

35. Lai,L.B., Vioque,A., Kirsebom,L.A. and Gopalan,V. (2010) Unexpected diversity of RNase P, an ancient tRNA processing enzyme: challenges and prospects. *FEBS Lett.*, **584**, 287–296.

36. Schenking,I., Hartmann,R.K. and Rossmanith,W. (2020) In: *Evolutionary Biology—A Transdisciplinary Approach*. Springer Nature Switzerland, pp. 255–299.

37. Guerrier-Takada,C., Gardiner,K., Marsh,T., Pace,N. and Altman,S. (1983) The RNA moiety of ribonuclease P is the catalytic subunit of the enzyme. *Cell*, **35**, 849–857.

38. Reiter,N.J., Osterman,A., Torres-Larios,A., Swinger,K.K., Pan,T. and Mondragon,A. (2010) Structure of a bacterial ribonuclease P holoenzyme in complex with tRNA. *Nature*, **468**, 784–789.

39. Lan,P., Tan,M., Zhang,Y., Niu,S., Chen,J., Shi,S., Qiu,S., Wang,X., Peng,X., Cai,G. *et al.* (2018) Structural insight into precursor tRNA processing by yeast ribonuclease P. *Science*, **362**, eaat6678.

40. Wan,F., Wang,Q., Tan,J., Tan,M., Chen,J., Shi,S., Lan,P., Wu,J. and Lei,M. (2019) Cryo-electron microscopy structure of an archaeal ribonuclease P. *Nat. Commun.*, **10**, 2617.

41. Wu,J., Niu,S., Tan,M., Huang,C., Li,M., Song,Y., Wang,Q., Chen,J., Shi,S., Lan,P. *et al.* (2018) Cryo-EM structure of the human ribonuclease P holoenzyme. *Cell*, **175**, 1393–1404.

42. Guerrier-Takada,C. and Altman,S. (1992) Reconstitution of enzymatic activity from fragments of M1 RNA. *Proc. Natl Acad. Sci. U.S.A.*, **89**, 1266–1270.

43. Loria,A. and Pan,T. (1996) Domain structure of the ribozyme from eubacterial ribonuclease P. *RNA*, **2**, 551–563.

44. Massire,C., Jaeger,L. and Westhof,E. (1997) Phylogenetic evidence for a new tertiary interaction in bacterial RNase P RNAs. *RNA*, **3**, 553–556.

45. Torres-Larios,A., Swinger,K.K., Krasilnikov,A.S., Pan,T. and Mondragon,A. (2005) Cystal structure of the RNA component of bacterial ribonuclease P. *Nature*, **437**, 584–587.

46. Lai,L.B., Chan,P.P., Cozen,A.E., Bernick,D.L., Brown,J.W., Gopalan,V. and Lowe,T.M. (2010) Discovery of a minimal form of RNase P in Pyrobaculum. *Proc. Natl Acad. Sci. U.S.A.*, **107**, 22493–22498.

47. Hall,T.A. and Brown,J.W. (2002) Archaeal RNase P has multiple protein subunits homologous to eukaryotic nuclear RNase P proteins. *RNA*, **8**, 296–306.

48. Boomershine,W.P., McElroy,C.A., Tsai,H.Y., Wilson,R.C., Gopalan,V. and Foster,M.P. (2003) Structure of Mth11/Mth Rpp29, an essential protein subunit of archaeal and eukaryotic RNase P. *Proc. Natl Acad. Sci. U.S.A.*, **100**, 15398–15403.

49. Kouzuma,Y., Mizoguchi,M., Takagi,H., Fukuhara,H., Tsukamoto,M., Numata,T. and Kimura,M. (2003) Reconstitution of archaeal ribonuclease P from RNA and four protein components. *Biochem. Biophys. Res. Commun.*, **306**, 666–673.

50. Lai,S.M., Lai,L.B., Foster,M.P. and Gopalan,V. (2014) The L7Ae protein binds to two kink-turns in the Pyrococcus furiosus RNase P RNA. *Nucleic Acids Res.*, **42**, 13328–13338.

51. Ma,X., Lai,L.B., Lai,S.M., Tanimoto,A., Foster,M.P., Wysocki,V.H. and Gopalan,V. (2014) Uncovering the stoichiometry of Pyrococcus furiosus RNase P, a multi-subunit catalytic ribonucleoprotein complex, by surface-induced dissociation and ion mobility mass spectrometry. *Angew. Chem. Int. Ed. Engl.*, **53**, 11483–11487.

52. Misra,V.K. and Draper,D.E. (1999) On the role of magnesium ions in RNA stability. *Biopolymers*, **48**, 113–135.

53. Strulson,C.A., Boyer,J.A., Whitman,E.E. and Bevilacqua,P.C. (2014) Molecular crowders and cosolutes promote folding cooperativity of RNA under physiological ionic conditions. *RNA*, **20**, 331–347.

54. Ward,W.L., Plakos,K. and DeRose,V.J. (2014) Nucleic acid catalysis: metals, nucleobases, and other cofactors. *Chem. Rev.*, **114**, 4318–4342.

55. Warnecke,J.M., Furste,J.P., Hardt,W.D., Erdmann,V.A. and Hartmann,R.K. (1996) Ribonuclease P (RNase P) RNA is converted to a Cd(2+)-ribozyme by a single Rp-phosphorothioate modification in the precursor tRNA at the RNase P cleavage site. *Proc. Natl Acad. Sci. U.S.A.*, **93**, 8924–8928.

56. Steitz,T.A. and Steitz,J.A. (1993) A general two-metal-ion mechanism for catalytic RNA. *Proc. Natl Acad. Sci. U.S.A.*, **90**, 6498–6502.

57. Brannvall,M., Kikovska,E., Wu,S. and Kirsebom,L.A. (2007) Evidence for induced fit in bacterial RNase P RNA-mediated cleavage. *J. Mol. Biol.*, **372**, 1149–1164.

58. Mao,G., Srivastava,A.S., Wu,S., Kosek,D., Lindell,M. and Kirsebom,L.A. (2018) Critical domain interactions for type A RNase P RNA catalysis with and without the specificity domain. *PLoS One*, **13**, e0192873.

59. Sinapah,S., Wu,S., Chen,Y., Pettersson,B.M., Gopalan,V. and Kirsebom,L.A. (2011) Cleavage of model substrates by archaeal RNase P: role of protein cofactors in cleavage-site selection. *Nucleic Acids Res.*, **39**, 1105–1116.

60. Wu,S., Chen,Y., Lindell,M., Mao,G. and Kirsebom,L.A. (2011) Functional coupling between a distal interaction and the cleavage site in bacterial RNase-P-RNA-mediated cleavage. *J. Mol. Biol.*, **411**, 384–396.

61. Hsieh,J. and Fierke,C.A. (2009) Conformational change in the Bacillus subtilis RNase P holoenzyme–pre-tRNA complex enhances substrate affinity and limits cleavage rate. *RNA*, **15**, 1565–1577.

62. Niland,C.N., Anderson,D.R., Jankowsky,E. and Harris,M.E. (2017) The contribution of the C5 protein subunit of Escherichia coli ribonuclease P to specificity for precursor tRNA is modulated by proximal 5′ leader sequences. *RNA*, **23**, 1502–1511.

63. Sun,L., Campbell,F.E., Zahler,N.H. and Harris,M.E. (2006) Evidence that substrate-specific effects of C5 protein lead to uniformity in binding and catalysis by RNase P. *EMBO J.*, **25**, 3998–4007.

64. Kazantsev,A.V., Rambo,R.P., Karimpour,S., Santalucia,J. Jr, Tainer,J.A. and Pace,N.R. (2011) Solution structure of RNase P RNA. *RNA*, **17**, 1159–1171.

65. Schroeder,K.T. and Lilley,D.M. (2009) Ion-induced folding of a kink turn that departs from the conventional sequence. *Nucleic Acids Res.*, **37**, 7281–7289.

66. VanAernum,Z.L., Gilbert,J.D., Belov,M.E., Makarov,A.A., Horning,S.R. and Wysocki,V.H. (2019) Surface-Induced dissociation of noncovalent protein complexes in an extended mass range orbitrap mass spectrometer. *Anal. Chem.*, **91**, 3611–3618.

67. Harvey,S.R., VanAernum,Z.L., Kostelic,M.M., Marty,M.T. and Wysocki,V.H. (2020) Probing the structure of nanodiscs using surface-induced dissociation mass spectrometry. *Chem. Commun. (Camb.)*, **56**, 15651–15654.

68. Vioque,A., Arnez,J. and Altman,S. (1988) Protein-RNA interactions in the RNase P holoenzyme from Escherichia coli. *J. Mol. Biol.*, **202**, 835–848.

69. Clegg,R.M. (1992) Fluorescence resonance energy transfer and nucleic acids. *Methods Enzymol.*, **211**, 353–388.

70. Donovan,B.T., Chen,H., Jipa,C., Bai,L. and Poirier,M.G. (2019) Dissociation rate compensation mechanism for budding yeast pioneer transcription factors. *Elife*, **8**, e43008.

71. Soltermann,F., Foley,E.D.B., Pagnoni,V., Galpin,M., Benesch,J.L.P., Kukura,P. and Struwe,W.B. (2020) Quantifying protein-protein Interactions by molecular counting with mass photometry. *Angew. Chem. Int. Ed. Engl.*, **59**, 10774–10779.

72. Sonn-Segev,A., Belacic,K., Bodrug,T., Young,G., VanderLinden,R.T., Schulman,B.A., Schimpf,J., Friedrich,T., Dip,P.V., Schwartz,T.U. *et al.* (2020) Quantifying the heterogeneity of macromolecular machines by mass photometry. *Nat. Commun.*, **11**, 1772.

73. Pomeranz Krummel,D.A. and Altman,S. (1999) Verification of phylogenetic predictions in vivo and the importance of the tetraloop motif in a catalytic RNA. *Proc. Natl Acad. Sci. U.S.A.*, **96**, 11200–11205.

74. Kirsebom,L.A. and Trobro,S. (2009) RNase P RNA-mediated cleavage. *IUBMB Life*, **61**, 189–200.

75. Cech,T.R. (2009) Crawling out of the RNA world. *Cell*, **136**, 599–602.

76. Johnson,K.A. (2008) Role of induced fit in enzyme specificity: a molecular forward/reverse switch. *J. Biol. Chem.*, **283**, 26297–26301.